JCTC Journal of Chemical Theory and Computation

pubs.acs.org/JCTC Article

Photoinduced Dynamics with Constrained Vibrational Motion: FrozeNM Algorithm

H. Negrin-Yuvero, V. M. Freixas, B. Rodriguez-Hernandez, G. Rojas-Lorenzo, S. Tretiak, A. Bastida, and S. Fernandez-Alberti*

Cite This: J. Chem. Theory Comput. 2020, 16, 7289−7298 Read Online

ACCESS | Metrics & More | Article Recommendations | Supporting Information

ABSTRACT: Ab initio molecular dynamics (AIMD) simulation, analyzed in terms of vibrational normal modes, is a widely used technique that facilitates understanding of complex structural motions and coupling between electronic and nuclear degrees of freedom. Usually, only a subset of vibrations is directly involved in the process of interest. The impact of these vibrations can be evaluated by performing AIMD simulations by selectively freezing certain motions. Herein, we present frozen normal mode (FrozeNM), a new algorithm to apply normal-mode constraints in AIMD simulations, as implemented in the nonadiabatic excited state molecular dynamics code. We further illustrate its capacity by analyzing the impact of normal-mode constraints on the photoinduced energy transfer between polyphenylene ethynylene dendrimer building blocks. Our results show that the electronic relaxation can be significantly slowed down by freezing a well-selected small subset of active normal modes characterized by their contributions in the direction of energy transfer. The application of these constraints reduces the nonadiabatic coupling between electronic excited states during the entire dynamical simulations. Furthermore, we validate reduced dimensionality models by freezing all the vibrations, except a few active modes. Altogether, we consider FrozeNM as a useful tool that can be broadly used to underpin the role of vibrational motion in a studied process and to formulate reduced models that describe essential physical phenomena.

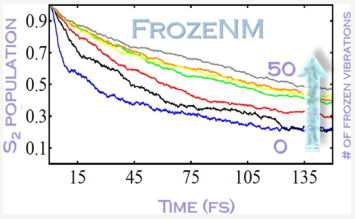

1. INTRODUCTION

Design of new functional molecular and solid materials frequently benefits from identification of a few coupled electronic and structural degrees of freedom that dominantly participate in the key physicochemical processes and are associated with desired functions. Examples include charge and energy transfer, nonradiative relaxation, molecular stability, and reactivity, to name a few. On the other hand, extensive atomistic details offered by modern simulations, such as ab initio molecular dynamics (AIMD) modeling, may hinder determination of the reduced set of variables, given the complexity of the entire manifold of nuclear motions. Within this context, an elaborate analysis of AIMD simulations in terms of vibrational normal modes helps to elucidate this issue.

Equilibrium normal modes (ENMs), typically calculated from the second derivatives of the ground-state (GS) energy with respect to nuclear coordinates, are extensively used to identify relevant vibrational motions of polyatomic molecules.[1−5] In particular, infrared and Raman spectroscopy measurements are usually interpreted in terms of vibrational band assignments associated with frequencies of these ENMs.[6−12] Because ENMs are obtained at the equilibrium geometry of the minimum of the ground-state potential energy surface (PES), they can be subjected to reordering and transient mixing during molecular dynamics (MD) even at room temperature.[13,14] Despite that, they have typically preserved the general average features of their identities, making ENMs a major tool for analyzing complex dynamics behavior in a large variety of biological and chemical systems.[15] In most cases, only a selected subset of ENMs, the so-called active normal modes, are the ones directly involved in the physical process of interest, for example, enzyme catalysis, protein conformational changes, and photoinduced dynamics in molecules. Different techniques have been developed to analyze these relevant vibrations.[16−20] On the one hand, the identification of active normal modes lends useful chemical insights into specific structure−property relationships that can guide the manipulation of desired technological or biological molecular functionalities. On the other hand, it allows to build and assess models of reduced dimensionality potentials that are necessary for high fidelity simulations including nuclear quantum effects that include these dominating nuclear motions.[20,21] Once the most important normal modes are identified, their impact on the selected aspects of dynamics can be explored by performing AIMD simulations by selectively freezing them.

Received: September 8, 2020
Published: November 17, 2020

https://dx.doi.org/10.1021/acs.jctc.0c00930
J. Chem. Theory Comput. 2020, 16, 7289−7298

In the realm of excited state dynamics, ENMs have also shown to be useful when analyzing vibrational energy redistribution pathways during ultrafast nonequilibrium processes such as photoinduced electron and energy transfer in conjugated chromophores.[22−27] However, a somewhat better description of these processes involving several coupled electronic excited states would require the use of state-specific normal modes. For this purpose, excited-state equilibrium normal modes (ES-ENMs), calculated at the minimum of the corresponding ES PESs, are convenient coordinates to describe internal conversion processes and characterize specific PESs features such as conical intersections.[28,29]

A large variety of methods have been developed to perform structure-constraint MD simulations, particularly by freezing bond length, angle, or dihedral angles.[30−43] Nevertheless, none of them has been extended to routinely freeze specific normal modes. Herein, we propose a new algorithm, called frozen normal mode (FrozeNM), to apply normal-mode constraints in MD simulations. The algorithm is an extension of RATTLE,[30] a "velocity" version of the SHAKE[31] algorithm for MD simulations. While both SHAKE and RATTLE have been originally developed to constrain bond length, and angles, FrozeNM aims to include ENM constraints. Similar to RATTLE, our method is based on the Velocity Verlet algorithm using Cartesian coordinates. FrozeNM guarantees that a selected set of collective coordinates, that is, normal modes, satisfy the required constraints at each time step. FrozeNM has been implemented in the nonadiabatic excited state molecular dynamics (NEXMD) computational package,[44,45] which is freely available at GitHub. The Non-adiabatic EXcited state molecular dynamics (NEXMD) Program code, license, and documentation may be accessed at https://github.com/lanl/NEXMD.

To illustrate a practical example, we further use FrozeNM to analyze the impact of normal mode constraints on the photoinduced nonadiabatic energy transfer between polyphenylene ethynylene (PPE) dendrimer building blocks. The NEXMD code has been previously successfully applied to simulate the intramolecular electronic and vibrational energy relaxation and redistribution in many extended conjugated PPE dendrimers.[46−52] Herein, we consider a simple model system 23PPE shown in Figure 1a, composed of two- and three-ring linear PPE chromophore units linked through metasubstitution. This molecular system is composed of building blocks present in more complex light harvesting dendrimers, such as the nanostar.[53−57] The metabranching localizes excitations within each linear fragment. These dendrimers have been shown to undergo highly efficient and unidirectional two-ring → three-ring electronic and vibrational energy transfer.[46−48] The ultrafast energy transfer takes place in the direction of the nonadiabatic couplings with the participation of a few ES active normal modes.[28,58] Thus, 23PPE is a good system for analyzing the normal mode contributions to the ultrafast nonadiabatic electronic energy relaxation that takes place after photoexcitation. We show that the electronic relaxation can be significantly slowed down by freezing a small subset of active normal modes characterized by their contributions in the direction of energy transfer, thus demonstrating the utility of the FrozeNM tool for various applications.

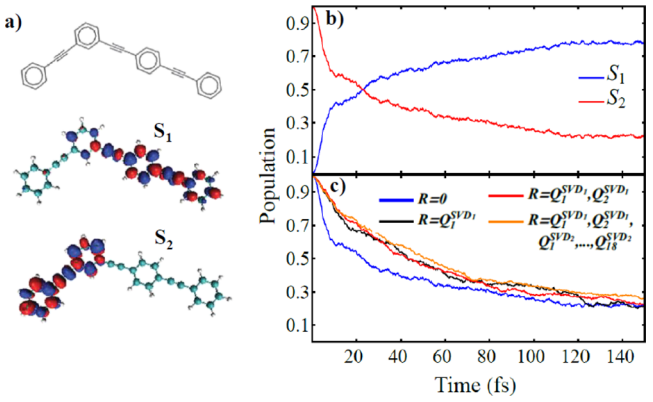

Figure 1. (a) Schematic representation of 23PPE-conjugated chromophore, the model dendritic molecule studied in this work. It is composed of two- and three-ring linear poly(phenylene ethynylene) units linked by metasubstitution. The localization of the electronic transition densities for S_1 and S_2 states at the ground-state minimum are also shown. (b) Time evolution of the populations of S_1 and S_2 electronic states averaged over an ensemble of trajectories as calculated by NEXMD without normal-mode constraints. (c) Comparison of the time evolution of the average population of the S_2 state for 23PPE obtained from NEXMD simulations. $R = 0$ indicates simulations without constraints. The ENMs that are frozen in each set of simulations are labeled using a superscript to indicate the singular value decomposition (SVD) vector and a subscript to indicate ith mode with the largest overlap with $\boldsymbol{d}_{12}^{\mathrm{SVD1/2}}$.

2. METHODS

2.1. Normal Mode Analysis. The ENM [$\{\mathbf{Q}_i\}$, (i = 1, ... $3N - 6$), N being the number of atoms in the molecule], and their frequencies ($\upsilon_i = (\sqrt{\lambda_i}/2\pi)$) are obtained from the eigenvector matrix $\mathbf{L}$ and eigenvalues [$\{\lambda_i\}$, (i = 1, ... $3N - 6$)] upon diagonalization, $\mathbf{L}^{\dagger}\mathbf{H}\mathbf{L} = \mathbf{\Lambda}$, of the corresponding mass-weighted Hessian matrix $\mathbf{H}$. The elements of $\mathbf{H}$ are defined as

$$H_{ij}(\boldsymbol{r}_0) = -\partial^2 E/\partial q_i \partial q_j|\boldsymbol{r}_0 \tag{1}$$

and they are evaluated at the equilibrium structure $\boldsymbol{r}_0$, obtained after performing geometry optimization of a molecular system on a given electronic PES, being either ground or excited state. E is the corresponding potential energy and $q_{3i-2} = \sqrt{m_i}(x_i - x_{0,i})$, $q_{3i-1} = \sqrt{m_i}(y_i - y_{0,i})$ and $q_{3i} = \sqrt{m_i}(z_i - z_{0,i})$ are the mass weighted Cartesian displacements of the ith atom. Equilibrium coordinates $\boldsymbol{r}_{0,i} = (x_{0,i}, y_{0,i}, z_{0,i})$ are defined in a *body-fixed* reference frame, with the origin at the center of mass of the molecule and axes corresponding to its principle axes of inertia.

The ENM amplitudes can be obtained throughout the MD simulation as a linear combination of the Cartesian coordinates as

$$Q_i(t) = \sum_{j=1}^{3N} l_{ji} q_j(t) = \sum_{j=1}^{3N} L_{ji} S_j(t) \qquad i = 1, \ldots, 3N - 6 \tag{2}$$

where l_{ji} are the elements of a matrix $\mathbf{L}$, and $L_{3i-x,j} = \sqrt{m_i} l_{3i-x,j}$ (x = 1, 2, 3), $S_{3i-2} = (x_i - x_{0,i})$, $S_{3i-1} = (y_i - y_{0,i})$, and $S_{3i} = (z_i - z_{0,i})$ are redefined elements of $\mathbf{L}$ and coordinates corresponding to the ith atom, respectively.

At this point, it is important to stress that MD simulations are commonly performed in the *space-fixed* Cartesian

https://dx.doi.org/10.1021/acs.jctc.0c00930
J. Chem. Theory Comput. 2020, 16, 7289−7298

coordinates. Matrix **L** is the linear transformation matrix that expresses the set of $\{\mathbf{Q}_i\}$ on the basis of $\{\mathbf{q}_i\}$ defined in the *body-fixed* Cartesian reference frame. Therefore, eq 2 requires that the Cartesian coordinates obtained from the MD simulations be erstwhile translated and rotated from the *space-fixed* to the *body-fixed* reference frame.

2.2. FrozeNM Algorithm. Consider a molecular system subject to R normal mode constraints that keep the j normal mode frozen at its initial value

$$\sigma_j(t) = Q_j(t) - Q_j(0) = \sum_{k=1}^{3N} L_{kj}\{S_k(t) - S_k(0)\} = 0 \quad (j = 1, \ldots, R) \tag{3}$$

The Newtonian equations of motions when applying the corresponding Lagrange multipliers λ_j can be written as

$$m_{S_i}\ddot{S}_i(t) = -\frac{\partial E}{\partial S_i} - \frac{\partial}{\partial S_i}\sum_{j=1}^{R}\lambda_j(t)\sigma_j(t), \quad (i = 1, \ldots, 3N) \tag{4}$$

where m_{S_i} corresponds to the mass of the ith atom associated to S_i, and we assume one Lagrange multiplier associated with each jth ENM.

Considering that

$$\frac{\partial \sigma_j(t)}{\partial S_i} = \frac{\partial}{\partial S_i}\sum_{k=1}^{3N} L_{kj}(S_k(t) - S_k(0)) = L_{ij}, \quad (j = 1, \ldots, R;\ i = 1, \ldots, 3N) \tag{5}$$

Equation 4 can be written as

$$m_{S_i}a_i(t) = F_i(t) - \sum_{j=1}^{R}\lambda_j(t)L_{ij}, \qquad (i = 1, \ldots, 3N) \tag{6}$$

with $a_i(t)$ being the acceleration, and the force $F_i(t)$ along the trajectory $\boldsymbol{r}(t)$ is defined as $-\frac{\partial E(\boldsymbol{r}(t))}{\partial S_i}$.

According to the velocity Verlet algorithm, the unrestricted S_i^{u} displacements at each time step Δt are calculated as

$$S_i^{\mathrm{u}}(t + \Delta t) = S_i(t) + v_i(t)\Delta t + \frac{\Delta t^2 F_i(t)}{2m_{S_i}}, \quad (i = 1, \ldots, 3N) \tag{7}$$

where $v_i(t)$ is the velocity in the direction of $S_i(t)$. When adding constraints, we obtain

$$S_i(t + \Delta t) = S_i^{\mathrm{u}}(t + \Delta t) - \frac{\Delta t^2}{2m_{S_i}}\sum_{j=1}^{R}\lambda_j(t)L_{ij}, \quad (i = 1, \ldots, 3N) \tag{8}$$

Because the normal mode constraints (eq 3) must be valid at any time during the propagation, using eqs 7 and 8, we can write

$$\begin{aligned}\sigma_j(t + \Delta t) &= Q_j(t + \Delta t) - Q_j(t)\\ &= \sum_{k=1}^{3N} L_{kj}\left\{v_k(t)\Delta t + \frac{\Delta t^2 F_k(t)}{2m_{S_k}}\right\} - \frac{\Delta t^2}{2}\sum_{i=1}^{R}\lambda_i(t)\\ &\sum_{k=1}^{3N}\frac{L_{kj}L_{ki}}{m_{S_k}} = 0, \qquad (j = 1, \ldots, R)\end{aligned} \tag{9}$$

and using the orthogonality of the **L** matrix, $\sum_{k=1}^{3N} l_{kj}l_{ki} = \sum_{k=1}^{3N} L_{kj}m_{S_k}^{-1}L_{ki} = \delta_{ji}$, we obtain

$$\lambda_j(t) = 2\Delta t^{-2}\sum_{k=1}^{3N} L_{kj}\left\{v_k(t)\Delta t + \frac{\Delta t^2 F_k(t)}{2m_{S_k}}\right\}, \quad (j = 1, \ldots, R) \tag{10}$$

In the velocity Verlet algorithm, the new velocities are obtained as

$$v_i(t + \Delta t) = v_i(t) + \frac{1}{2}(a_i(t) + a_i(t + \Delta t))\Delta t, \quad (i = 1, \ldots, 3N) \tag{11}$$

So that, using eq 6, we can write

$$v_i(t + \Delta t) = v_i(t) + \frac{\Delta t}{2m_{S_i}}\left\{(F_i(t) + F_i(t + \Delta t)) - \sum_{j=1}^{R} L_{ij}(\lambda_j(t) + \lambda_j(t + \Delta t))\right\}, \qquad (i = 1, \ldots, 3N) \tag{12}$$

As it has been pointed out in the ref 30, eq 12 cannot be used to obtain $v_i(t + \Delta t)$ because $\lambda_j(t + \Delta t)$ cannot be obtained with a simple iterative scheme as the one underpinning the Verlet algorithm. In order to overcome this issue, the RATTLE[30] algorithm propose to define $\lambda_j(t + \Delta t) = \gamma_j(t)$, and eq 12 can be written as

$$v_i(t + \Delta t) = v_i^{\mathrm{u}}(t + \Delta t) - \frac{\Delta t}{2m_{S_i}}\sum_{j=1}^{R} L_{ij}(\lambda_j(t) + \gamma_j(t)), \quad (i = 1, \ldots, 3N) \tag{13}$$

where the unrestricted velocities are given by

$$v_i^{\mathrm{u}}(t + \Delta t) = v_i(t) + \frac{\Delta t}{2m_{S_i}}(F_i(t) + F_i(t + \Delta t)) \tag{14}$$

In order to calculate the values of $\gamma_j(t)$, the ENM velocities can be obtain using eq 2 as

$$\dot{Q}_i(t + \Delta t) = \sum_{k=1}^{3N} L_{ki}v_k(t + \Delta t), \qquad (i = 1, \ldots, 3N) \tag{15}$$

Using the fact that $\dot{Q}_i(t + \Delta t) = 0$ for the R ENM constraints and substituting eq 13 in 15, we finally obtain

$$\gamma_j(t) = 2\Delta t^{-1}\sum_{k=1}^{3N} L_{kj}v_k^{\mathrm{u}}(t + \Delta t) - \lambda_j(t), \quad (j = 1, \ldots, R) \tag{16}$$

https://dx.doi.org/10.1021/acs.jctc.0c00930
J. Chem. Theory Comput. 2020, 16, 7289−7298

Altogether, eqs 8, 10, 13, and 16 summarize the application of the FrozeNM algorithm.

2.3. Computational Details. The photoexcitation and subsequent electronic relaxation of the 23PPE molecular system (see Figure 1a) have been simulated using the NEXMD package.[44,45] NEXMD combines the surface hopping algorithm[59,60] with "on the fly" analytical calculations of excited state energies, gradients, and nonadiabatic coupling terms at the configuration interaction singles (CIS) level with the semiempirical Hamiltonian models, as was detailed elsewhere.[45] Here, we use the AM1 model.[61]

Within the NEXMD framework, while nuclei are propagated classically with the Newtonian equations of motions (eq 4), the electronic wave function $\psi(t) = \sum_\alpha c_\alpha(t)\phi_\alpha$ is propagated quantum-mechanically using the basis of adiabatic electronic states ϕ_α

$$i\hbar\dot{c}_\alpha(t) = c_\alpha(t)E_\alpha - i\hbar\sum_\beta c_\beta(t)v\cdot d_{\alpha\beta} \tag{17}$$

here, E_α is the energy of the α^{th} electronic excited state, and $\boldsymbol{d}_{\alpha\beta}$ are the nonadiabatic derivative coupling vectors defined as $\boldsymbol{d}_{\alpha\beta} = \langle\phi_\alpha|\nabla_r\phi_\beta\rangle$. Details of the NEXMD approach, implementation, advantages, and testing parameters can be found in our previous works.[44,45]

The NEXMD simulations were performed on the 23PPE molecular system at constant energy. Initial conditions were collected from 1 ns of an equilibrated ground-state molecular dynamics simulation at 300 K with the Langevin friction coefficient γ = 20.0 ps^{-1}. For each set of selected ENM constraints, 600 individual NEXMD trajectories were started from these initial configurations by instantaneously promoting the system to the second excited state S_2. A classical time step of 0.5 fs has been used for nucleus propagation in the ground-state dynamics.

For excited-state dynamics simulations, a classical time step of 0.1 fs has been used for nucleus propagation, and a quantum time step of 0.025 fs has been used to propagate the electronic coefficients. Specific treatments of decoherence,[62] and trivial unavoided crossings[63] have been applied. According to the surface hopping prescription,[59,64,65] adjustments to the nuclear velocities are required in order to conserve total energy following hops between electronic states. The direction in which the velocity $v_i(t)$ of each of the ith atom in the molecular system is commonly rescaled, corresponds to the direction of the $\boldsymbol{d}_{\alpha\beta}$. In order to avoid the effect that these rescalings could have on the intramolecular vibrational flux during electronic relaxation, atomic velocities were rescaled in the same directions as they were at the time step before the hopping event occured.[22]

3. RESULTS AND DISCUSSION

Normal-mode constraint dynamics has been applied to the electronic energy relaxation process after photoexcitation of 23PPE. The molecule is initially excited to its S_2-excited singlet state localized on a two-ring linear segment that then relaxes to the lower-energy S_1 state localized on the three-ring segment.[46−48] Figure 1a indicates that S2 and S1 states are mostly localized on the two-ring and three-ring linear PPE units. Therefore, the $S_2 \rightarrow S_1$ electronic energy relaxation involves a two-ring → three-ring energy redistribution. Figure 1b shows the evolution in time of the average populations on S_1 and S_2 states obtained from unconstraint nonadiabatic MD simulations, that is, without the use of FrozeNM algorithms, allowing participation of all vibrational normal modes. As was previously reported,[46] an ultrafast transfer of the electronic population can be seen from the initially populated S_2 state to the lower-state S_1 on the timescale of around hundreds of femtoseconds.

We next perform constraint nonadiabatic MD simulations using the FrozeNM tool. As it has been pointed out previously,[28,45] $\boldsymbol{d}_{12}$ (see Section 2.3) represents the direction of the effective $S_2 \rightarrow S_1$ vibronic energy transfer. Therefore, we analyze the effect of systematically introducing constraints into ENMs according to their contribution to this vector. For this purpose, a representative $\boldsymbol{d}_{12}^{SVD}$ vector associated with the $S_2 \rightarrow S_1$ transition is defined by constructing a matrix $\mathbf{A}$ of dimension $3N \times K$, with K being the number of NEXMD trajectories featuring an effective $S_2 \rightarrow S_1$ transition. We define an effective $S_2 \rightarrow S_1$ transition, or a hop, as the last $S_2 \rightarrow S_1$ transition without further $S_1 \rightarrow S_2$ back-hopping during the rest of the trajectory dynamics. Matrix $\mathbf{A}$ is built with columns representing the $\boldsymbol{d}_{12}$ at the moment of effective $S_2 \rightarrow S_1$ transition in each of the K NEXMD trajectories. Matrix $\mathbf{A}$ represents a numerical characterization of nonadiabatic coupling vectors at a conical intersection seam sampled by an ensemble of MD trajectories. Thereafter, SVD of matrix $\mathbf{A}$ is performed, that is, $\mathbf{A}$ is written as

$$\mathbf{A} = \mathbf{U}\cdot\mathbf{W}\cdot\mathbf{V}^T \tag{18}$$

where matrix $\mathbf{U}$ is a $3N \times K$ column-orthogonal matrix, and $\mathbf{V}$ and $\mathbf{W}$ are $K \times K$ column-orthogonal and diagonal matrices, respectively. We denote $\boldsymbol{d}_{12}^{SVD1}$ and $\boldsymbol{d}_{12}^{SVD2}$ as the first and second columns of matrix $\mathbf{U}$ with the associated largest values of w_i (shown in Figure 2a,b). These two vectors can describe more

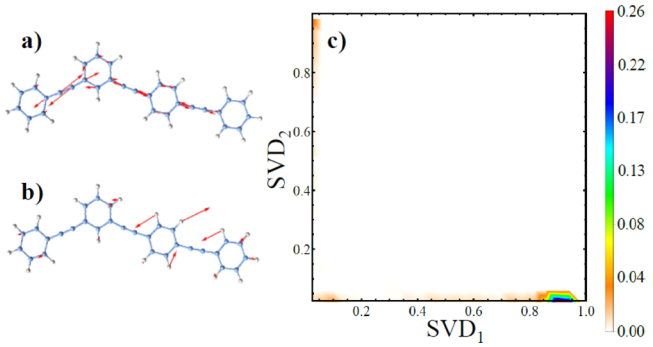

Figure 2. (a) $\boldsymbol{d}_{12}^{SVD1}$, (b) $\boldsymbol{d}_{12}^{SVD2}$, and (c) density plot of the overlap of each of the $\boldsymbol{d}_{12}$ from the ensemble with $\boldsymbol{d}_{12}^{SVD1}$ versus the overlap with $\boldsymbol{d}_{12}^{SVD2}$. The bar color in the right indicates probability density.

than 80% contribution of the original $\boldsymbol{d}_{12}$ vectors from the ensemble and 74% if only $\boldsymbol{d}_{12}^{SVD1}$ is taken into account. Therefore, they can be considered as dominating representatives of the entire set. This is reflected in Figure 2c, where the overlap between each $\boldsymbol{d}_{12}$ and $\boldsymbol{d}_{12}^{SVD1}$ versus the overlap between the same $\boldsymbol{d}_{12}$ and $\boldsymbol{d}_{12}^{SVD2}$ is depicted. $\boldsymbol{d}_{12}^{SVD1}$ shows a good representation of the majority of the original $\boldsymbol{d}_{12}$ vectors, and only a minority of them are expressed by $\boldsymbol{d}_{12}^{SVD2}$. $\boldsymbol{d}_{12}^{SVD1}$ and $\boldsymbol{d}_{12}^{SVD2}$ vectors can be interpreted as leading nonadiabatic couplings, characteristic for spatial localization of donor and acceptor states, respectively. As it has been pointed out in the previous study,[46] the major contributions to $\boldsymbol{d}_{12}^{SVD1}$ come from the stretching motions in the direction of the ethynylene bonds, especially the bonds corresponding to the two-ring

https://dx.doi.org/10.1021/acs.jctc.0c00930
J. Chem. Theory Comput. 2020, 16, 7289−7298

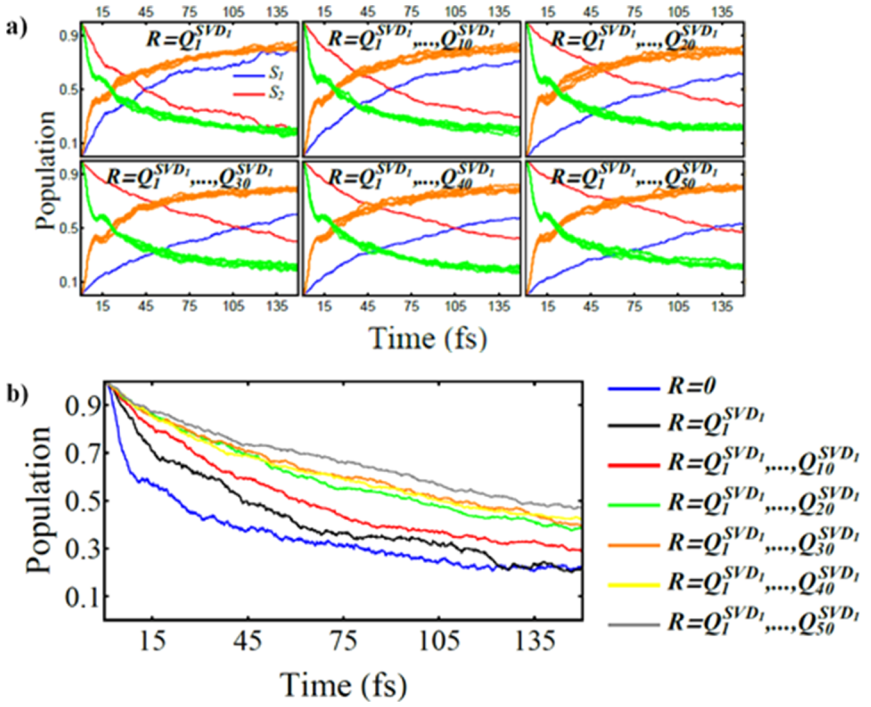

Figure 3. (a) Time evolution of the average populations of S_1 and S_2 electronic states calculated with a different subset R of the ENM constraints selected in the decreasing order of overlap with $\boldsymbol{d}_{12}^{SVD1}$. The ENMs that are frozen in each set of simulations are labeled using a subscript to indicate ith mode with the largest overlap with $\boldsymbol{d}_{12}^{SVD1}$. Populations of S_1 (yellow) and S_2 (green) states obtained from 10 new sets of NEXMD simulations with constraints performed over reference subsets of R randomly selected modes are also shown. (b) Comparison of time evolution of the average population of the S_2 state for the different constraint simulations.

linear unit. Besides, the delocalization of $\boldsymbol{d}_{12}^{SVD1}$ between the two-ring and three-ring linear PPE units allows the coupling between the two differently localized S_1 and S_2 states (see Figure 1a).

The FrozeNM algorithm can be applied to either GS- or excited-state normal modes (ES-ENM(S_α), α = 0, 1, 2). We note that ES-ENM(S_2) allows to achieve better representations of $\boldsymbol{d}_{12}$ (i.e., less number of ENMs are involved in the dynamics) compared to ES-ENM(S_1) or ENM(S_0) because the nonadiabatic coupling is particularly strong at the minimum of S_2 (because it is close to the conical intersection seam) affecting the normal mode structure.[28] Therefore, in the present work, we conduct the FrozeNM-constraint NEXMD simulations using ES-ENM(S_2) and, for the sake of simplicity, denote the latter as ENM. The complete list of c_i values, obtained by projecting $\boldsymbol{d}_{12}^{SVD1}$ and $\boldsymbol{d}_{12}^{SVD2}$ onto the basis of ES-ENM(S_2), is provided in Table S1 of Supporting Information

A further inspection of $\boldsymbol{d}_{12}^{SVD1}$ and $\boldsymbol{d}_{12}^{SVD2}$ can be performed by projecting them onto the ENM basis set

$$\boldsymbol{d}_{12} = \sum_{i=1}^{3N-6} c_i \mathbf{Q}_i \tag{19}$$

with $c_i = \boldsymbol{d}_{12}\cdot\mathbf{Q}_i$. The participation number (PN) of these projections is given by[66,67]

$$\mathrm{PN} = \left(\sum_{i=1}^{3N-6} (c_i)^4 \right)^{-1} \tag{20}$$

PN represents the number of ENMs that contribute to $\boldsymbol{d}_{12}$. Values of PN $\approx 3N - 6$ indicate the fully delocalized $\boldsymbol{d}_{12}$ with contributions from every ENM, whereas PN $\approx$ 1 corresponds to $\boldsymbol{d}_{12}$, being identical to a unique ENM. PN values of 1.3 and 17.3 have been obtained for $\boldsymbol{d}_{12}^{SVD1}$ and $\boldsymbol{d}_{12}^{SVD2}$, respectively, indicating that at least 1−2 and 17−18 ENMs are required to represent these vectors. Therefore, in order to analyze the impact that these directions of nuclear motions have on the $S_2 \rightarrow S_1$ energy transfer timescales, NEXMD simulations have been performed constraining the first and second ENMs that overlap the most with $\boldsymbol{d}_{12}^{SVD1}$ (i.e., those with the largest values of $(c_i)^2$, see eq 19) and the 18 ENMs that overlap the most with $\boldsymbol{d}_{12}^{SVD2}$. The obtained results are shown in Figure 1c. Here, in order to clarify which ENMs are frozen, we labeled them using a superscript to indicate the SVD vector and subscript to ith mode with the largest overlap with $\boldsymbol{d}_{12}^{SVD1/2}$. We can observe a significant impact of these ENM constraints at earlier times of the electronic relaxation immediately after photoexcitation. Nevertheless, the freezing of other modes than the one with the largest overlap with $\boldsymbol{d}_{12}^{SVD1}$ seems not to have further effects. This is a consequence of two features. On the one hand, the 144th ENM, which overlaps the most with $\boldsymbol{d}_{12}^{SVD1}$, presents a significant overlap (0.94) with $\boldsymbol{d}_{12}^{SVD1}$, while the second largest overlap (42nd ENM) is only 0.11 (see Table S1). Therefore, the impact of the latter on the main direction of electronic relaxation is expected to be less. On the other hand, $\boldsymbol{d}_{12}^{SVD2}$ represents only a minority of the original $\boldsymbol{d}_{12}$ vectors, and, therefore, its impact on the electronic relaxation is also expected to be less. After the first ∼80 fs of dynamics, the molecular system seems to find different segments of the conical intersection seam.

In order to further explore the effect of ENM constraints on the electronic relaxation of 23PPE, we have performed NEXMD simulations while gradually increasing number R of ENM constraints selected according to the decreasing order of values for ENM overlaps with $\boldsymbol{d}_{12}^{SVD1}$ (see Table S1). The initial configurations for these new sets of simulations were the same

https://dx.doi.org/10.1021/acs.jctc.0c00930
J. Chem. Theory Comput. 2020, 16, 7289−7298

original 600 configurations selected for the unconstraint NEXMD simulations. The effect of constraints over each of these selected set of R active normal modes has been statistically validated by comparing with results obtained by freezing an equivalent R number of randomly selected modes. For each R subset of modes, 10 new subsets of R randomly selected modes were built. These new subsets were considered as references, and for each of them, 600 individual NEXMD trajectories have been performed with the same initial configurations. Figure 3 shows that the electronic relaxation slows down significantly with the number of the ENM constraints when they are selected in the decreasing order of overlap with $\boldsymbol{d}_{12}^{\mathrm{SVD1}}$. The resulting half-life (i.e., time required for the S_2 population to reach a value of 0.5) values is 23.1, 43.1, 60.6, 98.3, 109.9, 107.3, and 132.9 fs for unconstrained and ENM constraint simulations with 1, 10, 20, 30, 40, and 50 frozen modes, respectively. This is not the case for subsets of randomly selected ENMs, where the corresponding average half-lives remain the same as for the unconstrained dynamics across the entire series 22.0 ± 1.5 fs. That is, the observed slowdown is related to a systematic closure of relaxation pathways rather than the simple reduction of the nuclear degrees of freedom serving as an effective bath for large molecules.

The observed slowdown in the electronic relaxation for the ENM constraint simulations can be analyzed in terms of the changes in the relative values of the nonadiabatic coupling between S_1 and S_2 states. According to eq 20, the evolution in time of the electronic populations is dictated by the coupling term $\mathrm{NACT}_{12} = \boldsymbol{v}\cdot\boldsymbol{d}_{12}$. Therefore, freezing those normal modes that contribute the most to $\boldsymbol{d}_{12}$ magnitude leads to decreased values of NACT_{12} with a subsequent reduction of the electronic population transfer rates between states. Figure 4

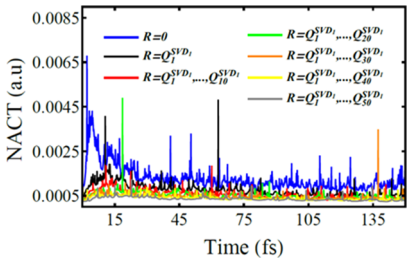

Figure 4. Time evolution of the average NACT_{12} calculated with different subset R of ENM constraints selected in the decreasing order of overlap with $\boldsymbol{d}_{12}^{\mathrm{SVD1}}$.

shows the evolution in time of NACT_{12} calculated during the different ENM constraint simulations. We can observe an initial significant decrease of the coupling in ENM constraint simulations with respect to unconstraint ones. Besides, throughout the simulations, we confirm the gradual decrease of NACT_{12} as R increases. Notably, the spikes in the behavior of this quantity are relevant to the near-degenerate energies of S_1 and S_2 states, evidencing that the trajectory is sampling the conical intersection seam. We further observe in Figure 4 that these spikes persist even for constrained simulations despite the reduced rates of appearance. This means that the dynamics is still able to sample different segments of seams of conical intersection when some vibrational coordinates are frozen.

At this point, it is interesting to analyze the effect of the ENM constraint dynamics on the vibrational energy flux that takes place concomitantly to the electronic energy transfer and relaxation. Vibrational kinetic energy $K(t)$ can be decomposed into individual contributions $K_i(t)$ of each ENM as

$$K(t) = \sum_{j=1}^{3N-6} K_i(t) = \frac{1}{2}\sum_{j=1}^{3N-6} (\dot{\mathbf{Q}}_i(t))^2 \tag{21}$$

and the total vibrational energy associated with a given ENM is obtained from the virial theorem, $E_i(t) = 2K_i(t)$. Figure 5a,b shows the average vibrational energies $E_i(t)$ for individual normal modes at the moment of effective $S_2 \rightarrow S_1$ transition (t_{hop}). Besides the 144th ENM, a bundle of active ENMs with frequencies (υ_i) in the range of ∼ [1790, 2470] cm^{-1} (i.e. 121th to 125th ENMs) have values of $E_i(t) > kT$. This situation changes once the 144th mode is constrained because the excess of energy on this bundle of modes significantly decreases. That is, freezing the 144th ENM not only affects the vibrational flux in this direction but also leads to a vibrational energy redistribution with less participation of the previously identified bundle of active modes. A further insight can be gained by analyzing the average $E_i(t)$ as a function of delay time, $\tau = t - t_{\mathrm{hop}}$, relative to the effective $S_2 \rightarrow S_1$ transition. This is shown in Figure 5c,d for a few selected active modes. We observe that the 144th ENM (with an average overlap of 0.94 with the direction of coupling between states, see Table S1) acts as a donor mode whose energy is transferred to the 121th to 125th bundle of acceptor ENMs after $S_2 \rightarrow S_1$ transition. Once the 144th ENM is frozen, these modes cannot further receive an excess of electronic energy with the same efficiency as before, leading to a less-efficient electronic and vibrational energy transfer.

The ENM constraint simulations allow us to directly measure the impact of hindering specific vibrations on the studied dynamical process. As an alternative to this procedure, we can analyze the effect of freezing vibrations that are not relevant to the dynamical process of interest and, therefore, test models of reduced dimensionality. For this purpose, we have performed the ENM constraint simulations in which all but a few ENM were frozen, that is, calculations considering only a few nuclear degrees of freedom. Figure 6 shows the results obtained by freezing all ENMs except those previously frozen in Figure 3 to exemplify a case when the molecular system is allowed to move along only a few selective nuclear degrees of freedom. We start with analysis of a simple situation when only a single nuclear degree of freedom is unfrozen. When only the 144th ENM (which has the largest overlap with $\boldsymbol{d}_{12}^{\mathrm{SVD1}}$) participates, we observe an efficient electronic relaxation but being still slower compared to the unrestricted simulation shown in Figure 6a. As a reference, Figure 6a also displays the results for another 10 sets of simulations starting with the same 600 initial configurations as those selected for the original set, where only a single randomly selected normal mode was enabled. As expected, no electronic relaxation is found on the ultrafast timescales for these 10 reference simulations. Therefore, the direction of $\boldsymbol{d}_{12}^{\mathrm{SVD1}}$ dictates the majority of the nonadiabatic transitions. Previous works[28] have explored the conical intersection topography in the energy difference gradient and nonadiabatic coupling vector branching plane for these types of PPE dendrimer building blocks, revealing a conical intersection seam in the direction of the nonadiabatic coupling vector. Figure 6b points out that by systematically increasing the number of participating ENMs selected in decreasing order of overlap with $\boldsymbol{d}_{12}^{\mathrm{SVD1}}$, only around 20 modes (i.e., 14% of the total nuclear degrees of freedom) are

https://dx.doi.org/10.1021/acs.jctc.0c00930
J. Chem. Theory Comput. 2020, 16, 7289−7298

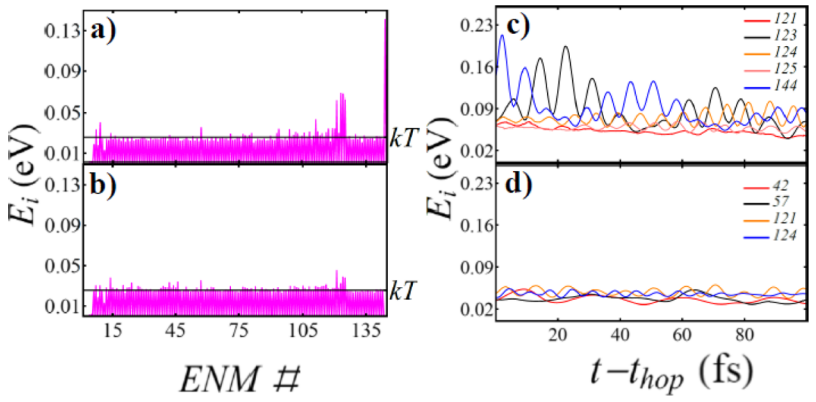

Figure 5. (a,b) Average vibrational energies E_i at the moment of effective $S_2 \rightarrow S_1$ transitions calculated without constraints when constraining the 144th ENM (i.e., the ENM with the largest overlap with $\boldsymbol{d}_{12}^{SVD1}$), respectively. (c,d) Average vibrational energies E_i of active modes during the NEXMD simulations as a function of delay time, $\tau = t - t_{hop}$, relative to the moment of nonadiabatic $S_2 \rightarrow S_1$ transition, calculated without constraints and when constraining the 144th ENM, respectively.

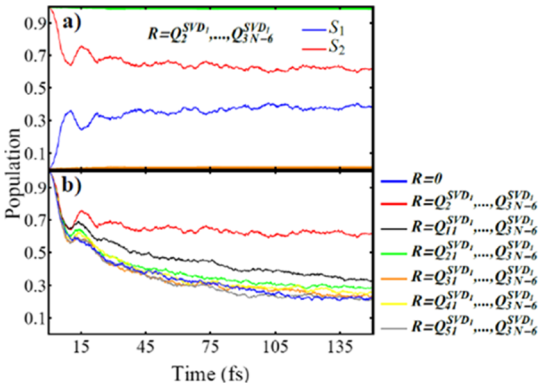

Figure 6. (a) Time evolution of the average populations of S_1 and S_2 states when the dynamics involve only a single nuclear degree of freedom. As reference, populations of S_1 (yellow) and S_2 (green) states are shown for simulations where one randomly selected ENM remains unfrozen. (b) Comparison of time evolution of the average population of the S_2 state for different constraint simulations when only R nuclear degrees of freedom are constrained.

necessary to achieve a reasonable qualitative agreement with the full-dimension simulations.

4. CONCLUSIONS

The new FrozeNM algorithm has been developed to include normal-mode constraints in AIMD simulations. The method extends the RATTLE[30] algorithm and can be straightforwardly applied to the velocity Verlet propagator that integrates the equations of motions in Cartesian coordinates. FrozeNM guarantees that a selected set of collective coordinates, that is, normal modes, satisfy the required constraints at each time step.

The utility of the presented algorithm has been shown by analyzing the impact of normal-mode constraints on the ultrafast energy transfer and electronic relaxation after photoexcitation of a model molecular system composed of PPE dendrimer building blocks. Our results demonstrate that the relaxation rates can be significantly reduced by freezing a well-defined small subset of active normal modes characterized by their contribution to the nonadiabatic coupling vector aligned with the direction of energy transfer. This effect is not observed for constraining a randomly selected normal-mode subset.

The FrozeNM algorithm can be used as an efficient tool to discover the role of certain vibrations for specific molecular processes that are not easily identifiable by other procedures. Once the relevant normal modes are identified, their impact on selected aspects of molecular dynamics can be straightforwardly explored by performing constraint simulations, as shown by our application example. Moreover, FrozeNM is useful for guiding development of reduced dimensionality Hamiltonians that can be further used for more accurate treatment of nonadiabatic dynamics, such as exploiting nuclear quantum effects in the selected directions of motion.[20,21] However, it is important to mention that, in its current version, FrozeNM cannot be applied directly to photoinduced process involving electronic excited states in which ES-ENMs cannot be well defined, as it is the case for excited states lacking geometric minimum or where geometric minimum is in the direct vicinity of a conical intersection seam. Moreover, floppy molecules with shallow PESs and multiple conformational metastable minima may require careful definition of effective normal modes that fully exploit effectiveness of constraints. Overall, FrozeNM can be adapted to freeze an arbitrary set of collective vibrational coordinates, for instance, defined by a principal component analysis, among others.

The FrozeNM method can be easily implemented into arbitrary molecular dynamics computational packages, as demonstrated by its integration into a freely distributed NEXMD package. We believe that this tool is suitable for elucidating the role of vibrational motions and structural distortions in a dynamical process of interest and thus can be a helpful tool for in silico design of new materials or biosystems with tunable properties and desired functions.

■ ASSOCIATED CONTENT

Supporting Information

The Supporting Information is available free of charge at https://pubs.acs.org/doi/10.1021/acs.jctc.0c00930.

Absolute values of the overlap (inner product) of each ES-ENM(S_2) with $\boldsymbol{d}_{12}^{SVD1}$ and $\boldsymbol{d}_{12}^{SVD2}$ (PDF)

■ AUTHOR INFORMATION

Corresponding Author

S. Fernandez-Alberti − *Departamento de Ciencia y Tecnologia, Universidad Nacional de Quilmes/CONICET,*

https://dx.doi.org/10.1021/acs.jctc.0c00930
J. Chem. Theory Comput. 2020, 16, 7289−7298

Bernal B1876BXD, Argentina; orcid.org/0000-0002-0916-5069; Email: sfalberti@gmail.com

Authors

H. Negrin-Yuvero – *Departamento de Ciencia y Tecnologia, Universidad Nacional de Quilmes/CONICET, Bernal B1876BXD, Argentina*

V. M. Freixas – *Departamento de Ciencia y Tecnologia, Universidad Nacional de Quilmes/CONICET, Bernal B1876BXD, Argentina;* orcid.org/0000-0003-1733-4827

B. Rodriguez-Hernandez – *Departamento de Ciencia y Tecnologia, Universidad Nacional de Quilmes/CONICET, Bernal B1876BXD, Argentina*

G. Rojas-Lorenzo – *Departamento de Física Atómica y Molecular, Instituto Superior de Tecnologías y Ciencias Aplicadas, Universidad de La Habana, La Habana, Cuba;* orcid.org/0000-0002-7605-9426

S. Tretiak – *Theoretical Division, Center for Nonlinear Studies (CNLS), and Center for Integrated Nanotechnologies (CINT), Los Alamos National Laboratory, Los Alamos, New Mexico 87545, United States;* orcid.org/0000-0001-5547-3647

A. Bastida – *Departamento de Química Física, Universidad de Murcia, Murcia 30100, Spain;* orcid.org/0000-0002-8193-9233

Complete contact information is available at: https://pubs.acs.org/10.1021/acs.jctc.0c00930

Notes

The authors declare no competing financial interest.

■ ACKNOWLEDGMENTS

This work was partially supported by CONICET, UNQ, ANPCyT (PICT-2018-2360). The work at the Los Alamos National Laboratory (LANL) was performed in part at the Center for Integrated Nanotechnologies (CINT), a U.S. Department of Energy, Office of Science User Facility. This research used resources provided by the LANL Institutional Computing Program. This work has received financial support provided by the Spanish Agencia Estatal de Investigación (AEI) and Fondo Europeo de Desarrollo Regional (FEDER, UE) under project CTQ2016-79345-P and by the Fundación Séneca under project 20789/PI/18.

■ REFERENCES

(1) Brooks, III, C.; Karplus, M.; Pettitt, B. M. *Proteins: A Theoretical Perspective of Dynamics, Structure, and Thermodynamics, Advances I.*; Prigogine, I., Rice, S. A., Eds.; John Wiley & Sons Ltd, 1987.

(2) Nishikawa, T.; Gō, N. Normal Modes of Vibration in Bovine Pancreatic Trypsin Inhibitor and Its Mechanical Property. *Proteins: Struct., Funct., Genet.* **1987**, *2*, 308–329.

(3) Brooks, B.; Karplus, M. Harmonic Dynamics of Proteins: Normal Modes and Fluctuations in Bovine Pancreatic Trypsin Inhibitor. *Proc. Natl. Acad. Sci. U.S.A.* **1983**, *80*, 6571–6575.

(4) Andrew McCammon, J.; Harvey, S. C. *Dynamics of Proteins and Nucleic Acids*; Cambridge University Press, 1987.

(5) Brooks, C. L.; Karplus, M.; Pettitt, B. M. Proteins: A theoretical perspective of dynamics, structure, and thermodynamics. *Adv. Chem. Phys.* **1988**, *71*, 1–259.

(6) Hill, J. R.; Ziegler, C. J.; Suslick, K. S.; Dlott, D. D.; Rella, C. W.; Fayer, M. D. Tuning the Vibrational Relaxation of Co Bound to Heme and Metalloporphyrin Complexes. *J. Phys. Chem.* **1996**, *100*, 18023–18032.

(7) Peterson, K. a.; Rella, C. W.; Engholm, J. R.; Schwettman, H. a. Ultrafast Vibrational Dynamics of the Myoglobin Amide I Band. *J. Phys. Chem. B* **1999**, *103*, 557–561.

(8) Dlott, D. D. Vibrational energy redistribution in polyatomic liquids: 3D infrared-Raman spectroscopy. *Chem. Phys.* **2001**, *266*, 149–166.

(9) Fayer, M. *Ultrafast Infrared and Raman Spectroscopy*; Marcel Dekker Inc.: New York, 2001.

(10) Iwaki, L.; Dlott, D. Vibrational Energy Transfer in Condensed Phases. In *Encyclopedia of Chemical Physics and Physical Chemistry*; Moore, J., Spencer, N., Eds.; Taylor & Francis: Bristol, 2001; p 2717.

(11) Dresselhaus, M. S.; Dresselhaus, G.; Jorio, A. Molecular Vibrations, Infrared, and Raman Activity. *Group Theory*; Springer: Berlin, Heidelberg, 2008; pp 147–178.

(12) Hashimoto, K.; Badarla, V. R.; Kawai, A.; Ideguchi, T. Complementary Vibrational Spectroscopy. *Nat. Commun.* **2019**, *10*, 4411.

(13) Kalstein, A.; Fernández-Alberti, S.; Bastida, A.; Soler, M. A.; Farag, M. H.; Zúñiga, J.; Requena, A. Vibrational Dynamics of Polyatomic Molecules in Solution: Assignment, Time Evolution and Mixing of Instantaneous Normal Modes. *Theor. Chem. Acc.* **2011**, *128*, 769–782.

(14) Zgierski, M. Z. On Mode Mixing Effects in Absorption-Emission Spectra and Resonance Raman Excitation Profiles. *Chem. Phys.* **1986**, *108*, 61–68.

(15) *Normal Mode Analysis. Theory and Applications to Biological and Chemical Systems*; Cui, Q., Bahar, I., Eds.; Chapman & Hall/CRC: London, U.K., 2006.

(16) Mai, S.; González, L. Identification of Important Normal Modes in Nonadiabatic Dynamics Simulations by Coherence, Correlation, and Frequency Analyses. *J. Chem. Phys.* **2019**, *151*, 244115.

(17) Alfonso-Hernandez, L.; Athanasopoulos, S.; Tretiak, S.; Miguel, B.; Bastida, A.; Fernandez-Alberti, S. Vibrational Energy Redistribution during Donor-Acceptor Electronic Energy Transfer: Criteria to Identify Subsets of Active Normal Modes. *Phys. Chem. Chem. Phys.* **2020**, *22*, 18454–18466.

(18) Yang, X.; Bittner, E. R.; Yang, X.; Bittner, E. R. Computing Intramolecular Charge and Energy Transfer Rates Using Optimal Modes. *J. Chem. Phys.* **2015**, *142*, 244114.

(19) Lasorne, B.; Sicilia, F.; Bearpark, M. J.; Robb, M. A.; Worth, G. A.; Blancafort, L. Automatic generation of active coordinates for quantum dynamics calculations: Application to the dynamics of benzene photochemistry. *J. Chem. Phys.* **2008**, *128*, 124307–124317.

(20) Gómez, S.; Heindl, M.; Szabadi, A.; González, L. From Surface Hopping to Quantum Dynamics and Back. Finding Essential Electronic and Nuclear Degrees of Freedom and Optimal Surface Hopping Parameters. *J. Phys. Chem. A* **2019**, *123*, 8321–8332.

(21) Capano, G.; Penfold, T. J.; Chergui, M.; Tavernelli, I. Photophysics of a Copper Phenanthroline Elucidated by Trajectory and Wavepacket-Based Quantum Dynamics: A Synergetic Approach. *Phys. Chem. Chem. Phys.* **2017**, *19*, 19590–19600.

(22) Shenai, P. M.; Fernandez-Alberti, S.; Bricker, W. P.; Tretiak, S.; Zhao, Y. Internal Conversion and Vibrational Energy Redistribution in Chlorophyll A. *J. Phys. Chem. B* **2016**, *120*, 49–58.

(23) Kurtz, L.; Hofmann, A.; de Vivie-riedle, R. Ground state normal mode analysis: Linking excited state dynamics and experimental observables. *J. Chem. Phys.* **2001**, *114*, 6151–6159.

(24) Yang, X.; Keane, T.; Delor, M.; Meijer, A. J. H. M.; Weinstein, J.; Bittner, E. R. Identifying Electron Transfer Coordinates in Donor-Bridge-Acceptor Systems Using Mode Projection Analysis. *Nat. Commun.* **2017**, *8*, 14554.

(25) Yang, X.; Bittner, E. R. Intramolecular Charge- and Energy-Transfer Rates with Reduced Modes: Comparison to Marcus Theory for Donor-Bridge-Acceptor Systems. *J. Phys. Chem. A* **2014**, *118*, 5196–5203.

(26) Yang, X.; Pereverzev, A.; Bittner, E. R. Inelastic Charge-Transfer Dynamics in Donor-Bridge-Acceptor Systems Using Optimal Modes. *Adv. Chem. Phys.* **2018**, 167–194.

(27) Rodríguez-Hernández, B.; Oldani, N.; Martínez-Mesa, A.; Uranga-Piña, L.; Tretiak, S.; Fernandez-Alberti, S. Photoexcited energy relaxation and vibronic couplings in π-conjugated carbon nanorings. *Phys. Chem. Chem. Phys.* **2020**, *22*, 15321−15332.
(28) Soler, M. A.; Nelson, T.; Roitberg, A. E.; Tretiak, S.; Fernandez-Alberti, S. Signature of Nonadiabatic Coupling in Excited-State Vibrational Modes. *J. Phys. Chem. A* **2014**, *118*, 10372−10379.
(29) Sicilia, F.; Blancafort, L.; Bearpark, M. J.; Robb, M. A. Quadratic Description of Conical Intersections: Characterization of Critical Points on the Extended Seam. *J. Phys. Chem. A* **2007**, *111*, 2182−2192.
(30) Andersen, H. C. Rattle: A "velocity" version of the shake algorithm for molecular dynamics calculations. *J. Comput. Phys.* **1983**, *52*, 24−34.
(31) Ryckaert, J.-P.; Ciccotti, G.; Berendsen, H. J. C. Numerical Integration of the Cartesian Equations of Motion of a System with Constraints: Molecular Dynamics of n-Alkanes. *J. Comput. Phys.* **1977**, *23*, 327−341.
(32) Forester, T. R.; Smith, W. SHAKE, rattle, and roll: Efficient constraint algorithms for linked rigid bodies. *J. Comput. Chem.* **1998**, *19*, 102−111.
(33) Pechlaner, M.; van Gunsteren, W. Algorithms to Apply Dihedral-Angle Constraints in Molecular or Stochastic Dynamics Simulations. *J. Chem. Phys.* **2020**, *152*, 024109.
(34) Ciccotti, G.; Ferrario, M.; Ryckaert, J.-P. Molecular Dynamics of Rigid Systems in Cartesian Coordinates A General Formulation. *Mol. Phys.* **1982**, *47*, 1253−1264.
(35) Lambrakos, S. G.; Boris, J. P.; Oran, E. S.; Chandrasekhar, I.; Nagumo, M. A Modified Shake Algorithm for Maintaining Rigid Bonds in Molecular Dynamics Simulations of Large Molecules. *J. Comput. Phys.* **1989**, *85*, 473−486.
(36) Edberg, R.; Evans, D. J.; Morriss, G. P. Constrained Molecular Dynamics: Simulations of Liquid Alkanes with a New Algorithm. *J. Chem. Phys.* **1986**, *84*, 6933.
(37) Miyamoto, S.; Kollman, P. A. Settle: An Analytical Version of the SHAKE and RATTLE Algorithm for Rigid Water Models. *J. Comput. Chem.* **1992**, *13*, 952−962.
(38) Yoneya, M.; Berendsen, H. J. C.; Hirasawa, K. A Non-Iterative Matrix Method for Constraint Molecular Dynamics Simulations. *Mol. Simul.* **1994**, *13*, 395−405.
(39) Barth, E.; Kuczera, K.; Leimkuhler, B.; Skeel, R. D. Algorithms for Constrained Molecular Dynamics. *J. Comput. Chem.* **1995**, *16*, 1192−1209.
(40) Slusher, J. T.; Cummings, P. T. Non-Iterative Constraint Dynamics Using Velocity-Explicit Verlet Methods. *Mol. Simul.* **2006**, *18*, 213−224.
(41) Hess, B.; Bekker, H.; Berendsen, H. J. C.; Fraaije, J. G. E. M. LINCS: A Linear Constraint Solver for Molecular Simulations. *J. Comput. Chem.* **1997**, *18*, 1463−1472.
(42) Gonnet, P.; Walther, J. H.; Koumoutsakos, P. ϑ-SHAKE: An extension to SHAKE for the explicit treatment of angular constraints. *Comput. Phys. Commun.* **2009**, *180*, 360−364.
(43) Dubbeldam, D.; Oxford, G. A. E.; Krishna, R.; Broadbelt, L. J.; Snurr, R. Q. Distance and Angular Holonomic Constraints in Molecular Simulations. *J. Chem. Phys.* **2010**, *133*, 034114.
(44) Malone, W.; Nebgen, B.; White, A.; Zhang, Y.; Song, H.; Bjorgaard, J. A.; Sifain, A. E.; Rodriguez-Hernandez, B.; Freixas, V. M.; Fernandez-Alberti, S.; Roitberg, A. E.; Nelson, T. R.; Tretiak, S. NEXMD Software Package for Nonadiabatic Excited State Molecular Dynamics Simulations. *J. Chem. Theory Comput.* **2020**, *16*, 5771−5783.
(45) Nelson, T. R.; White, A. J.; Bjorgaard, J. A.; Sifain, A. E.; Zhang, Y.; Nebgen, B.; Fernandez-alberti, S.; Mozyrsky, D.; Roitberg, A. E.; Tretiak, S. Non-adiabatic Excited-State Molecular Dynamics: Theory and Applications for Modeling Photophysics in Extended Molecular Materials. *Chem. Rev.* **2020**, *120*, 2215−2287.
(46) Fernandez-Alberti, S.; Kleiman, V. D.; Tretiak, S.; Roitberg, A. E. Nonadiabatic Molecular Dynamics Simulations of the Energy Transfer between Building Blocks in a Phenylene Ethynylene Dendrimer†. *J. Phys. Chem. A* **2009**, *113*, 7535−7542.
(47) Fernandez-Alberti, S.; Kleiman, V. D.; Tretiak, S.; Roitberg, A. E. Unidirectional Energy Transfer in Conjugated Molecules: The Crucial Role of High-Frequency C≡C Bonds. *J. Phys. Chem. Lett.* **2010**, *1*, 2699−2704.
(48) Nelson, T.; Fernandez-Alberti, S.; Roitberg, A. E.; Tretiak, S. Nonadiabatic Excited-State Molecular Dynamics: Modeling Photophysics in Organic Conjugated Materials. *Acc. Chem. Res.* **2014**, *47*, 1155−1164.
(49) Fernandez-Alberti, S.; Roitberg, A. E.; Kleiman, V. D.; Nelson, T.; Tretiak, S. Shishiodoshi Unidirectional Energy Transfer Mechanism in Phenylene Ethynylene Dendrimers. *J. Chem. Phys.* **2012**, *137*, 22A526−22A535.
(50) Galindo, J. F.; Atas, E.; Altan, A.; Kuroda, D. G.; Fernandez-Alberti, S.; Tretiak, S.; Roitberg, A. E.; Kleiman, V. D. Dynamics of Energy Transfer in a Conjugated Dendrimer Driven by Ultrafast Localization of Excitations. *J. Am. Chem. Soc.* **2015**, *137*, 11637−11644.
(51) Ondarse-Alvarez, D.; Kömürlü, S.; Roitberg, A. E.; Pierdominici-Sottile, G.; Tretiak, S.; Fernandez-Alberti, S.; Kleiman, V. D. Ultrafast Electronic Energy Relaxation in a Conjugated Dendrimer Leading to Inter-Branch Energy Redistribution. *Phys. Chem. Chem. Phys.* **2016**, *18*, 25080−25089.
(52) Ondarse-Alvarez, D.; Oldani, N.; Roitberg, A. E.; Kleiman, V.; Tretiak, S.; Fernandez-Alberti, S. Energy Transfer and Spatial Scrambling of an Exciton in a Conjugated Dendrimer. *Phys. Chem. Chem. Phys.* **2018**, *20*, 29648−29660.
(53) Swallen, S. F.; Kopelman, R.; Moore, J. S.; Devadoss, C. Dendrimer photoantenna supermolecules: energetic funnels, exciton hopping and correlated excimer formation. *J. Mol. Struct.* **1999**, *485*−*486*, 585−597.
(54) Palma, J. L.; Atas, E.; Hardison, L.; Marder, T. B.; Collings, J. C.; Beeby, A.; Melinger, J. S.; Krause, J. L.; Kleiman, V. D.; Roitberg, A. E. Electronic Spectra of the Nanostar Dendrimer: Theory and Experiment. *J. Phys. Chem. C* **2010**, *114*, 20702−20712.
(55) Kopelman, R.; Shortreed, M.; Shi, Z.-Y.; Tan, W.; Xu, Z.; Moore, J. S.; Bar-Haim, A.; Klafter, J. Spectroscopic Evidence for Excitonic Localization in Fractal Antenna Supermolecules. *Phys. Rev. Lett.* **1997**, *78*, 1239.
(56) Devadoss, C.; Bharathi, P.; Moore, J. S. Energy Transfer in Dendritic Macromolecules: Molecular Size Effects and the Role of an Energy Gradient. *J. Am. Chem. Soc.* **1996**, *118*, 9635−9644.
(57) Shortreed, M. R.; Swallen, S. F.; Shi, Z.-Y.; Tan, W.; Xu, Z.; Devadoss, C.; Moore, J. S.; Kopelman, R. Directed Energy Transfer Funnels in Dendrimeric Antenna Supermolecules†. *J. Phys. Chem. B* **1997**, *101*, 6318−6322.
(58) Soler, M. A.; Roitberg, A. E.; Nelson, T.; Tretiak, S.; Fernandez-Alberti, S. Analysis of State-Specific Vibrations Coupled to the Unidirectional Energy Transfer in Conjugated Dendrimers. *J. Phys. Chem. A* **2012**, *116*, 9802−9810.
(59) Tully, J. C. Molecular Dynamics with Electronic Transitions. *J. Chem. Phys.* **1990**, *93*, 1061−1071.
(60) Hammes-schiffer, S.; Tully, J. C. Proton Transfer in Solution : Molecular Dynamics with Quantum Transitions. *J. Chem. Phys.* **1994**, *101*, 4657.
(61) Dewar, M. J. S.; Zoebisch, E. G.; Healy, E. F.; Stewart, J. J. P. Development and use of quantum mechanical molecular models. 76. AM1: a new general purpose quantum mechanical molecular model. *J. Am. Chem. Soc.* **1985**, *107*, 3902−3909.
(62) Nelson, T.; Fernandez-alberti, S.; Roitberg, A. E.; Tretiak, S. Nonadiabatic excited-state molecular dynamics: Treatment of electronic decoherence. *J. Chem. Phys.* **2013**, *138*, 224111.
(63) Fernandez-Alberti, S.; Roitberg, A. E.; Nelson, T.; Tretiak, S. Identification of Unavoided Crossings in Nonadiabatic Photoexcited Dynamics Involving Multiple Electronic States in Polyatomic Conjugated Molecules. *J. Chem. Phys.* **2012**, *137*, 014512.
(64) Tully, J. C. Nonadiabatic Molecular Dynamics. *Int. J. Quantum Chem.* **1991**, *40*, 299−309.

https://dx.doi.org/10.1021/acs.jctc.0c00930
J. Chem. Theory Comput. 2020, 16, 7289−7298

(65) Hack, M. D.; Jasper, A. W.; Volobuev, Y. L.; Schwenke, D. W.; Truhlar, D. G. Quantum Mechanical and Quasiclassical Trajectory Surface Hopping Studies of the Electronically Nonadiabatic Predissociation of the Ã State of NaH2. **1999**, *103*, 6309−6326. DOI: 10.1021/jp9912049

(66) Bell, R. J.; Dean, P.; Hibbins-Butler, D. C. Localization of normal modes in vitreous silica, germania and beryllium fluoride. *J. Phys. C: Solid State Phys.* **1970**, *3*, 2111−2118.

(67) Taraskin, S. N.; Elliott, S. R. Anharmonicity and Localization of Atomic Vibrations in Vitreous Silica. *Phys. Rev. B* **1999**, *59*, 8572−8585.

https://dx.doi.org/10.1021/acs.jctc.0c00930
J. Chem. Theory Comput. 2020, 16, 7289−7298